

Introduction to Seismology:
The wave equation and body waves

Peter M. Shearer
Institute of Geophysics and Planetary Physics
Scripps Institution of Oceanography
University of California, San Diego

Notes for CIDER class
June, 2010

Chapter 1

Introduction

Seismology is the study of earthquakes and seismic waves and what they tell us about Earth structure. Seismology is a data-driven science and its most important discoveries usually result from analysis of new data sets or development of new data analysis methods. Most seismologists spend most of their time studying *seismograms*, which are simply a record of Earth motion at a particular place as a function of time. Fig. 1.1 shows an example seismogram.

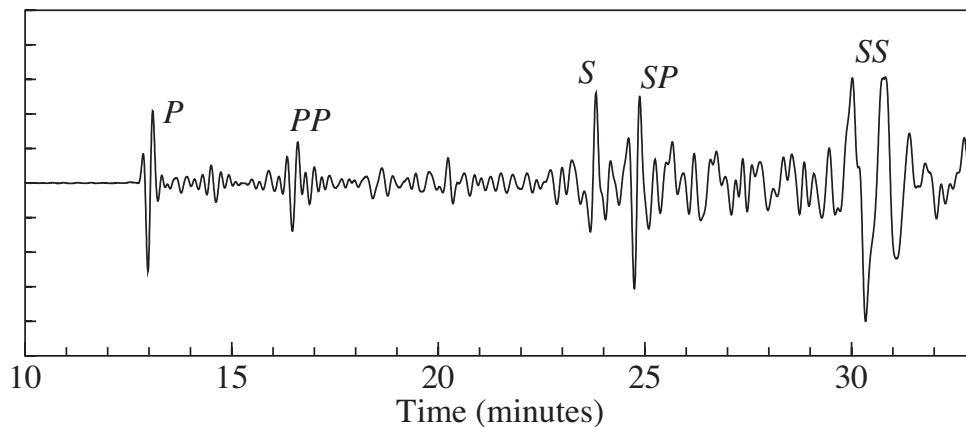


Figure 1.1: The 1994 Northridge earthquake recorded at station OBN in Russia. Some of the visible phases are labeled.

Modern seismograms are digitized at regular time intervals and analyzed on computers. Many concepts of time series analysis, including filtering and spectral methods, are valuable in seismic analysis. Although continuous background Earth “noise” is sometimes studied, most seismic analyses are of records of discrete sources of seismic wave energy, i.e., earthquakes and explosions. The appearance of these

seismic records varies greatly as a function of the source-receiver distance. The different distance ranges are often termed:

1. *Local* seismograms occur at distances up to about 200 km. The main focus is usually on the direct P waves (compressional) and S waves (shear) that are confined to Earth's crust. Analysis of data from the Southern California Seismic Network for earthquake magnitude and locations falls into this category. Surface waves are not prominent although they can sometimes be seen at very short periods.
2. *Regional* seismology studies examine waveforms from beyond ~ 200 up to 2000 km or so. At these distances, the first seismic arrivals travel through the upper mantle (below the Moho that separates the crust and mantle). Surface waves become more obvious in the records. Analysis of continent-sized data sets is an example of regional seismology, such as current USArray project to deploy seismometers across the United States.
3. *Global* seismology is at distances beyond about 2000 km ($\sim 20^\circ$), where seismic wave arrivals are termed *teleseisms*. This involves a multitude of body-wave phase arrivals, arising from reflected and phase-converted phases from the surface and the core-mantle boundary. For shallow sources, surface waves are the largest amplitude arrivals. Data come from the global seismic network (GSN).

The appearance of seismograms also will vary greatly depending upon how they are filtered. What seismologists term short-period records are usually filtered to frequencies above about 0.5 Hz. What seismologists term long-period records are filtered to below about 0.1 Hz (above 10 s period). Examples of short- and long-period waveform stacks are shown in Figs. 1.2 and 1.3. Note the different phases visible at the different periods.

You can learn a lot from a single seismogram. For example, if both P and S arrivals can be identified, then the $S - P$ time can be used to estimate the distance to the source. A rule of thumb in local seismology is that the distance in kilometers

Short-period (vertical)

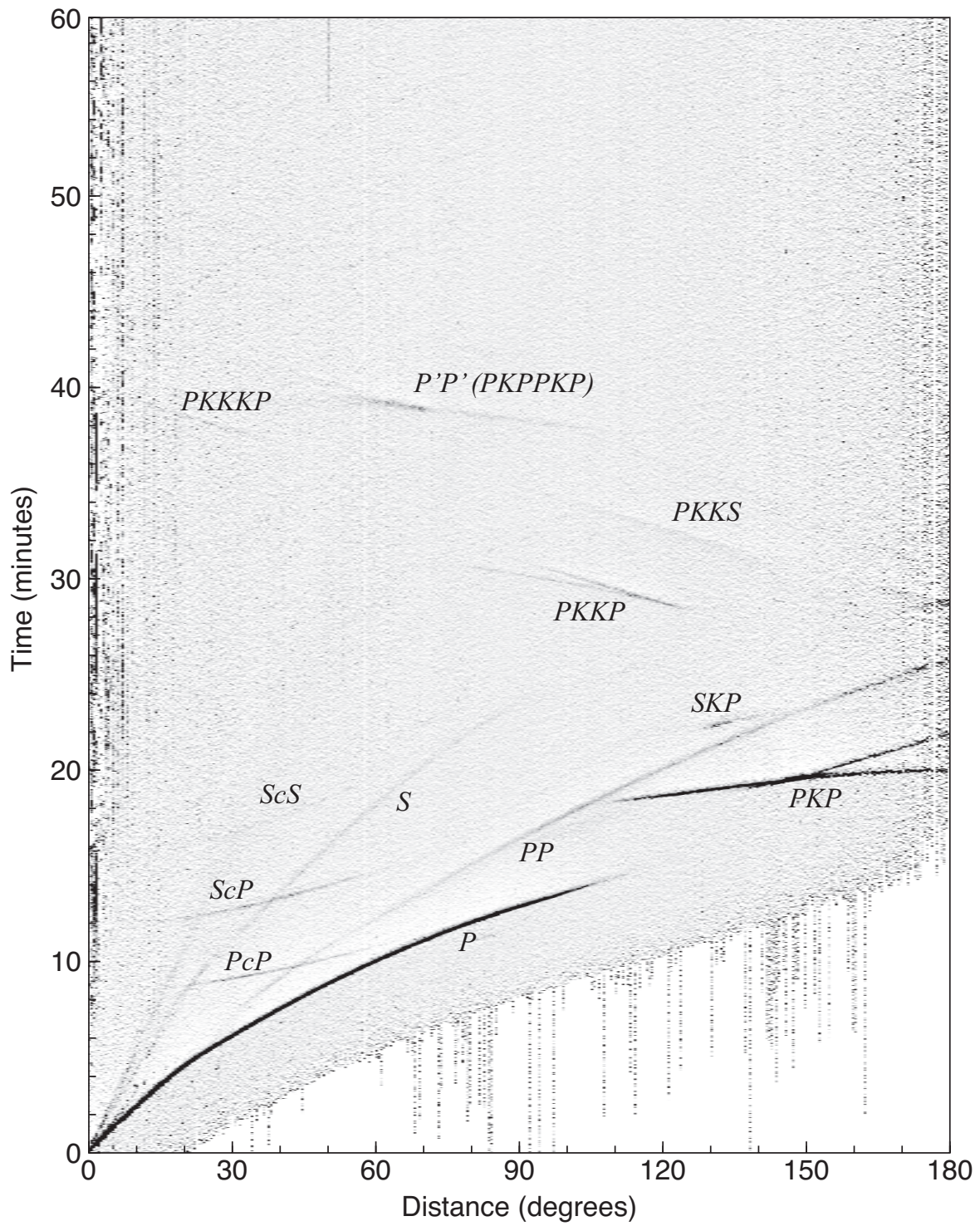


Figure 1.2: A stack of short-period (<2 s), vertical component data from the global networks between 1988 to 1994. (From Astiz et al., 1996.)

Long-period (vertical)

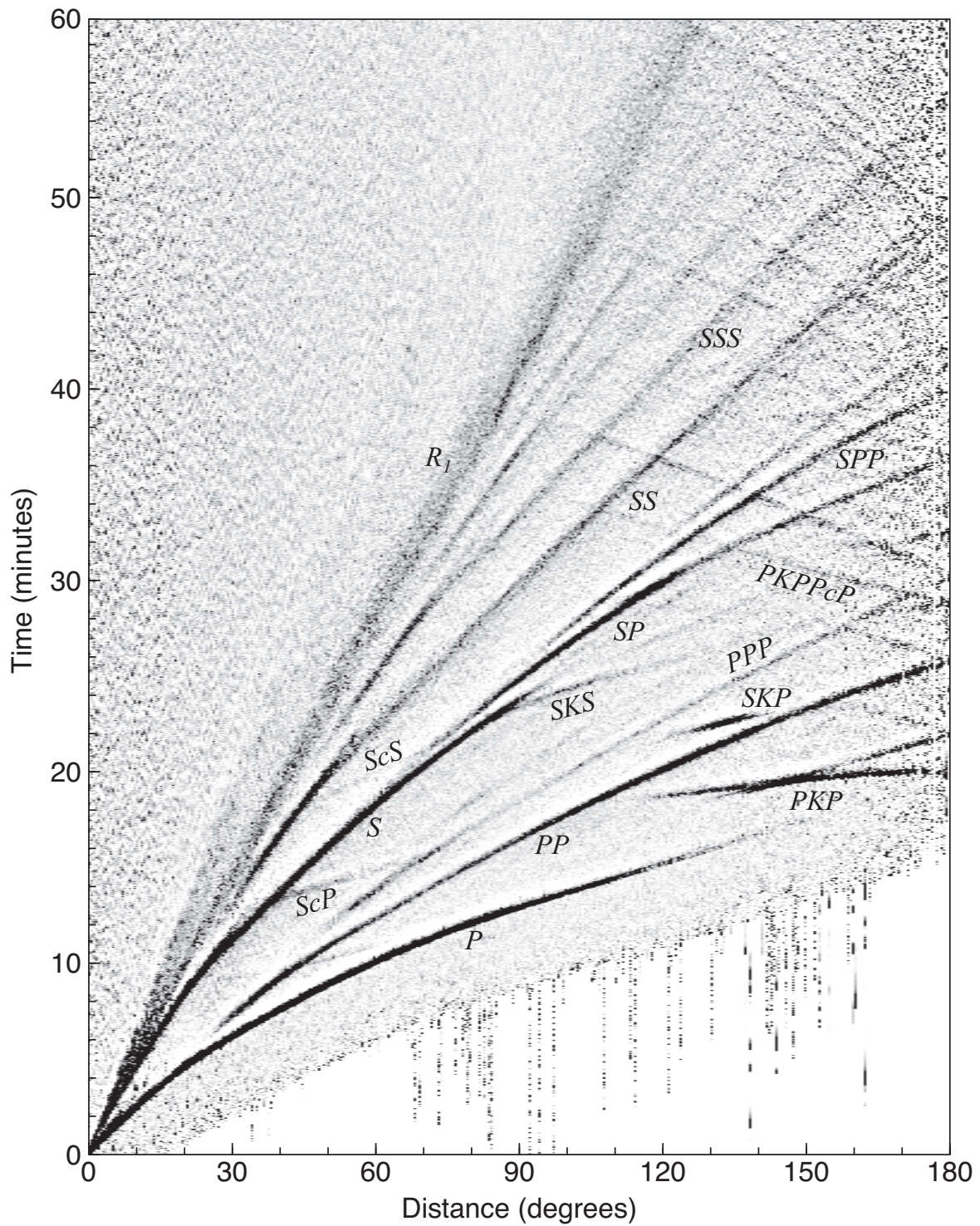


Figure 1.3: A stack of long-period (>10 s), vertical component data from the global networks between 1988 to 1994. (From Astiz et al., 1996.)

is about 8 times the $S-P$ time in seconds. Once the distance is known, the P - or S -wave amplitude can be used to estimate the event magnitude (S waves are usually used for local records, P waves in the case of teleseisms). In global seismology, surface wave *dispersion* (arrival times varying as a function of frequency) can be used to constrain seismic velocity as a function of depth.

You can learn more if you have a three-component (vertical and two orthogonal horizontal sensors) seismic station that fully characterizes the vector nature of ground motion. In this case, the angle that a seismic wave arrives at the station can be estimated, which permits an approximate source location to be determined. One can then separate the surface waves into Rayleigh waves (polarized in the source direction) and Love waves (polarized at right angles to the source direction). Sometimes the S arrival will be observed to be split into two orthogonal components of motion (see Fig. 1.4). This is called *shear-wave splitting* and is diagnostic of seismic anisotropy, in which wave speed varies as a function of direction in a material. The orientation and magnitude of the anisotropy can be estimated from shear-wave splitting observations. Sometimes, a weak S -wave arrival will be observed to follow the teleseismic P -wave arrival, which is caused by a P -to- S converted phase at the Moho (the crust-mantle boundary). The timing of this phase can be used to estimate crustal thickness.

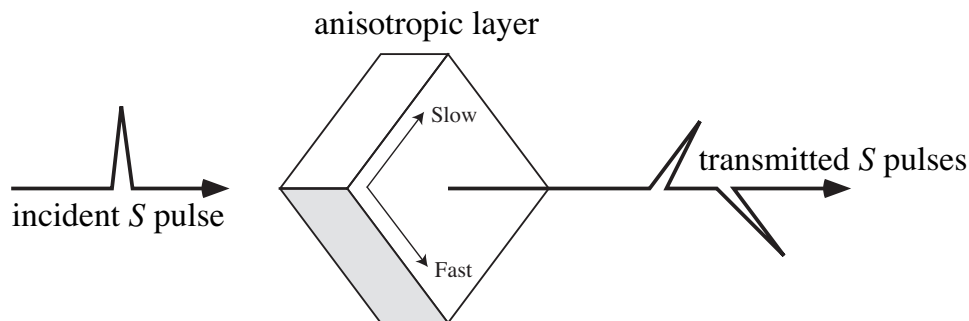


Figure 1.4: An S -wave that travels through an anisotropic layer can split into two S -waves with orthogonal polarizations; this is due to the difference in speed between the qS waves in the anisotropic material.

But much, much more can be learned when data from many different seismic stations are available. In the early days of seismology, seismic stations were rare and expensive and often operated separately by different institutions. But the impor-

tance of sharing data to determine accurate earthquake locations and Earth velocity structure was very clear. Thus seismology began a tradition of free and open sharing of data that continues to this day. This has been facilitated by centralized data repositories, initially just the arrival times and amplitudes measured by the different station operators, then to the actual seismograms themselves, as archived in film chip libraries, and eventually to modern digital seismic networks and data centers.

This data-sharing tradition is a very appealing part of being a seismologist. It's easy for any of us to obtain an abundance of data. All you have to do is go online to the appropriate data center (SCECDC for southern California, the IRIS DMC for GSN data). You don't have to know anybody there, you don't have to ask somebody to do you a favor to get the data, you don't have to collaborate with anybody. The data are simply there for you to use. Seismic networks are funded by the community for the entire community to use. Even data from PI-funded experiments to study particular regions typically are released 18 months after the experiment ends. Indeed, the National Science Foundation (NSF) requires that all data collected in NSF-funded experiments be made available through data centers. Furthermore, seismology is very data rich and most seismic data sets have not been fully analyzed. People are constantly discovering new things in old data sets.

This makes it possible for individual seismologists (and grad students) to make important contributions without having to get an experiment funded or to join part of some large team. Most published seismology papers have 1 to 4 authors. Compare that to the particle physics community! Other fields are starting to recognize the importance and power of data sharing. For example, the astronomy community is beginning to fund automated sky surveys where all of the data will immediately be available online. But seismology has a 100 year head start in open access data sharing.

1.1 References

Astiz, L., Earle, P., and Shearer, P. (1996). Global stacking of broadband seismograms, *Seismol. Res. Lett.*, **67**, 8–18.

Chapter 2

The seismic wave equation

The classical physics behind most of seismology starts with Newton's second law of motion

$$\mathbf{F} = m\mathbf{a} \quad (2.1)$$

where \mathbf{F} is the applied force, m is the mass, and \mathbf{a} is the acceleration. Generalized to a continuous medium¹, this equation becomes

$$\rho \frac{\partial^2 u_i}{\partial t^2} = \partial_j \tau_{ij} + f_i. \quad (2.2)$$

where ρ is the density, \mathbf{u} is the displacement, and $\boldsymbol{\tau}$ is the stress tensor. Note that i and j are assumed to range from 1 to 3 (for the x , y , and z directions) and we are using the notation $\partial_x u_y = \partial u_y / \partial x$. We also are using the *summation convention* in our index notation. Any repeated index in a product indicates that the sum is to be taken as the index varies from 1 to 3. Thus $\partial_j \tau_{ij} = \partial \tau_{ix} / \partial x + \partial \tau_{iy} / \partial y + \partial \tau_{iz} / \partial z$.

This is the fundamental equation that underlies much of seismology. It is called the *momentum equation* or the *equation of motion* for a continuum. Each of the terms, u_i , τ_{ij} and f_i is a function of position \mathbf{x} and time. The body force term \mathbf{f} generally consists of a gravity term \mathbf{f}_g and a source term \mathbf{f}_s . Gravity is an important factor at very low frequencies in normal mode seismology, but it can generally be neglected for body- and surface-wave calculations at typically observed wavelengths. In the absence of body forces, we have the *homogeneous equation of motion*

$$\rho \frac{\partial^2 u_i}{\partial t^2} = \partial_j \tau_{ij}, \quad (2.3)$$

¹see Chapter 3 of Introduction to Seismology for more details throughout this section.

which governs seismic wave propagation outside of seismic source regions. Generating solutions to (2.2) or (2.3) for realistic Earth models is an important part of seismology; such solutions provide the predicted ground motion at specific locations at some distance from the source and are commonly termed *synthetic seismograms*.

In order to solve (2.3) we require a relationship between stress and strain so that we can express $\boldsymbol{\tau}$ in terms of the displacement \mathbf{u} . Because strains associated with seismic waves are generally very small, we can assume a linear stress-strain relationship. The linear, isotropic² stress-strain relation is

$$\tau_{ij} = \lambda \delta_{ij} e_{kk} + 2\mu e_{ij}, \quad (2.4)$$

where λ and μ are the Lamé parameters and the strain tensor is defined as

$$e_{ij} = \frac{1}{2}(\partial_i u_j + \partial_j u_i). \quad (2.5)$$

Substituting for e_{ij} in (2.4), we obtain

$$\tau_{ij} = \lambda \delta_{ij} \partial_k u_k + \mu(\partial_i u_j + \partial_j u_i). \quad (2.6)$$

Equations (2.3) and (2.6) provide a coupled set of equations for the displacement and stress. These equations are sometimes used directly at this point to model wave propagation in computer calculations by applying finite-difference techniques. In these methods, the stresses and displacements are computed at a series of grid points in the model, and the spatial and temporal derivatives are approximated through numerical differencing. The great advantage of finite-difference schemes is their relative simplicity and ability to handle Earth models of arbitrary complexity. However, they are extremely computationally intensive and do not necessarily provide physical insight regarding the behavior of the different wave types.

Substituting (2.6) into (2.3), we may obtain

$$\rho \ddot{\mathbf{u}} = \nabla \lambda (\nabla \cdot \mathbf{u}) + \nabla \mu \cdot [\nabla \mathbf{u} + (\nabla \mathbf{u})^T] + (\lambda + 2\mu) \nabla \nabla \cdot \mathbf{u} - \mu \nabla \times \nabla \times \mathbf{u}. \quad (2.7)$$

This is one form of the *seismic wave equation*. The first two terms on the right-hand side (r.h.s.) involve gradients in the Lamé parameters themselves and are nonzero

²The Earth is not always isotropic, but isotropy is commonly assumed as a first-order approximation. The equations for anisotropic media are more complicated.

whenever the material is inhomogeneous (i.e., contains velocity gradients). Most non trivial Earth models for which we might wish to compute synthetic seismograms contain such gradients. However, including these factors makes the equations very complicated and difficult to solve efficiently. Thus, most practical synthetic seismogram methods ignore these terms, using one of two different approaches.

First, if velocity is only a function of depth, then the material can be modeled as a series of homogeneous layers. Within each layer, there are no gradients in the Lamé parameters and so these terms go to zero. The different solutions within each layer are linked by calculating the reflection and transmission coefficients for waves at both sides of the interface separating the layers. The effects of a continuous velocity gradient can be simulated by considering a “staircase” model with many thin layers. As the number of layers increases, these results can be shown to converge to the continuous gradient case (more layers are needed at higher frequencies). This approach forms the basis for many techniques for computing predicted seismic motions from one-dimensional Earth models.

Second, it can be shown that the strength of these gradient terms varies as $1/\omega$, where ω is frequency, and thus at high frequencies these terms will tend to zero. This approximation is made in most *ray-theoretical methods*, in which it is assumed that the frequencies are sufficiently high that the $1/\omega$ terms are unimportant. However, note that at any given frequency this approximation will break down if the velocity gradients in the material become steep enough. At velocity discontinuities between regions of shallow gradients, the approximation cannot be used directly, but the solutions above and below the discontinuities can be patched together through the use of reflection and transmission coefficients.

If we ignore the gradient terms, the momentum equation for homogeneous media becomes

$$\rho\ddot{\mathbf{u}} = (\lambda + 2\mu)\nabla\nabla \cdot \mathbf{u} - \mu\nabla \times \nabla \times \mathbf{u}. \quad (2.8)$$

This is a standard form for the seismic wave equation in homogeneous media and forms the basis for most body wave synthetic seismogram methods. However, it is important to remember that it is an approximate expression, which has neglected

the gravity and velocity gradient terms and has assumed a linear, isotropic Earth model.

We can separate this equation into solutions for P -waves and S -waves by taking the divergence and curl, respectively, and using several vector identities. The resulting P -wave equation is

$$\nabla^2(\nabla \cdot \mathbf{u}) - \frac{1}{\alpha^2} \frac{\partial^2(\nabla \cdot \mathbf{u})}{\partial t^2} = 0, \quad (2.9)$$

where the P -wave velocity, α , is given by

$$\alpha = \sqrt{\frac{\lambda + 2\mu}{\rho}}. \quad (2.10)$$

The corresponding S -wave equation is

$$\nabla^2(\nabla \times \mathbf{u}) - \frac{1}{\beta^2} \frac{\partial^2(\nabla \times \mathbf{u})}{\partial t^2} = 0, \quad (2.11)$$

where the S -wave velocity, β , is given by

$$\beta = \sqrt{\frac{\mu}{\rho}}. \quad (2.12)$$

For P -waves, the only displacement occurs in the direction of propagation along the x axis. Such wave motion is termed “longitudinal.” The motion is curl-free or “irrotational.” Since P -waves introduce volume changes in the material ($\nabla \cdot \mathbf{u} \neq 0$), they can also be termed “compressional” or “dilatational.” However, note that P -waves involve shearing as well as compression; this is why the P velocity is sensitive to both the bulk and shear moduli. Particle motion for a harmonic P -wave is shown in Figure 2.1.

For S -waves, the motion is perpendicular to the propagation direction. S -wave particle motion is often divided into two components: the motion within a vertical plane through the propagation vector (SV -waves) and the horizontal motion in the direction perpendicular to this plane (SH -waves). The motion is pure shear without any volume change (hence the name shear waves). Particle motion for a harmonic shear wave polarized in the vertical direction (SV -wave) is illustrated in Figure 2.1.

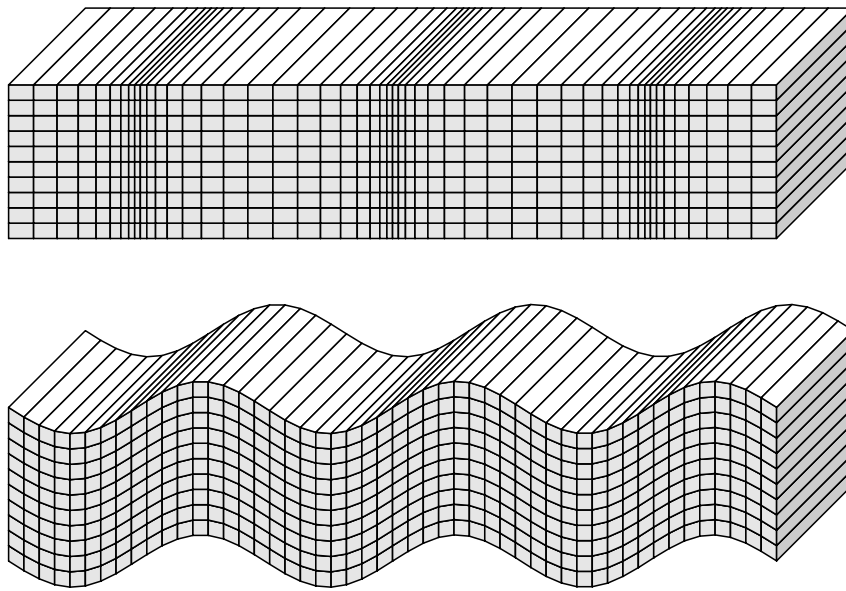


Figure 2.1: Displacements occurring from a harmonic plane P -wave (top) and S -wave (bottom) traveling horizontally across the page. S -wave propagation is pure shear with no volume change, whereas P -waves involve both a volume change and shearing (change in shape) in the material. Strains are highly exaggerated compared to actual seismic strains in the Earth.

Chapter 3

Ray theory

Seismic ray theory is analogous to optical ray theory and has been applied for over 100 years to interpret seismic data. It continues to be used extensively today, due to its simplicity and applicability to a wide range of problems. These applications include most earthquake location algorithms, body wave focal mechanism determinations, and inversions for velocity structure in the crust and mantle. Ray theory is intuitively easy to understand, simple to program, and very efficient. Compared to more complete solutions, it is relatively straightforward to generalize to three-dimensional velocity models. However, ray theory also has several important limitations. It is a high-frequency approximation, which may fail at long periods or within steep velocity gradients, and it does not easily predict any “nongeometrical” effects, such as head waves or diffracted waves. The ray geometries must be completely specified, making it difficult to study the effects of reverberation and resonance due to multiple reflections within a layer.

3.1 Snell’s Law

Consider a plane wave, propagating in material of uniform velocity v , that intersects a horizontal interface (Fig. 3.1).

The wavefronts at time t and time $t + \Delta t$ are separated by a distance Δs along the ray path. The ray angle from the vertical, θ , is termed the incidence angle. This angle relates Δs to the wavefront separation on the interface, Δx , by

$$\Delta s = \Delta x \sin \theta. \tag{3.1}$$

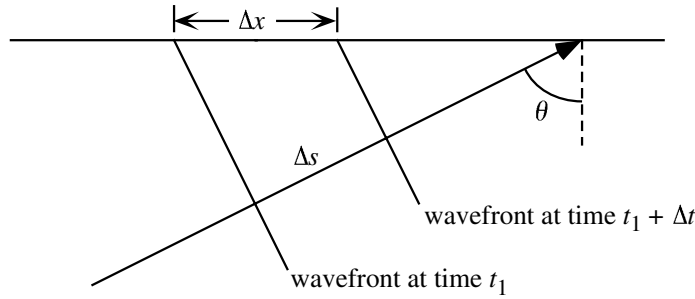


Figure 3.1: A plane wave incident on a horizontal surface. The ray angle from vertical is termed the incidence angle θ .

Since $\Delta s = v\Delta t$, we have

$$v\Delta t = \Delta x \sin \theta \quad (3.2)$$

or

$$\frac{\Delta t}{\Delta x} = \frac{\sin \theta}{v} = u \sin \theta \equiv p, \quad (3.3)$$

where u is the *slowness* ($u = 1/v$ where v is velocity) and p is termed the *ray parameter*. If the interface represents the free surface, note that by timing the arrival of the wavefront at two different stations, we could directly measure p . The ray parameter p represents the apparent slowness of the wavefront in a horizontal direction, which is why p is sometimes called the *horizontal slowness* of the ray.

Now consider a downgoing plane wave that strikes a horizontal interface between two homogeneous layers of different velocity and the resulting transmitted plane wave in the lower layer (Fig. 3.2). If we draw wavefronts at evenly spaced times along the ray, they will be separated by different distances in the different layers, and we see that the ray angle at the interface must change to preserve the

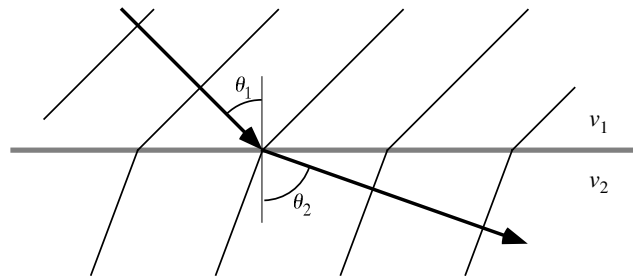


Figure 3.2: A plane wave crossing a horizontal interface between two homogeneous half-spaces. The higher velocity in the bottom layer causes the wavefronts to be spaced further apart.

timing of the wavefronts across the interface.

In the case illustrated the top layer has a slower velocity ($v_1 < v_2$) and a correspondingly larger slowness ($u_1 > u_2$). The ray parameter may be expressed in terms of the slowness and ray angle from the vertical within each layer:

$$p = u_1 \sin \theta_1 = u_2 \sin \theta_2. \quad (3.4)$$

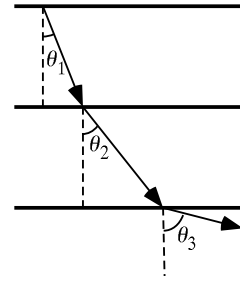
Notice that this is simply the seismic version of Snell's law in geometrical optics.

3.2 Ray Paths for Laterally Homogeneous Models

In most cases the compressional and shear velocities increase as a function of depth in the Earth. Suppose we examine a ray traveling downward through a series of layers, each of which is faster than the layer above. The ray parameter p remains constant and we have

$$p = u_1 \sin \theta_1 = u_2 \sin \theta_2 = u_3 \sin \theta_3. \quad (3.5)$$

If the velocity continues to increase, θ will eventually equal 90° and the ray will be traveling horizontally.



This is also true for continuous velocity gradients (Fig. 3.3). If we let the slowness at the surface be u_0 and the *takeoff angle* be θ_0 , we have

$$u_0 \sin \theta_0 = p = u \sin \theta. \quad (3.6)$$

When $\theta = 90^\circ$ we say that the ray is at its *turning point* and $p = u_{tp}$, where u_{tp} is the slowness at the turning point. Since velocity generally increases with depth in Earth, the slowness *decreases* with depth. Smaller ray parameters are more steeply dipping at the surface, will turn deeper in Earth, and generally travel farther. In these examples with horizontal layers or vertical velocity gradients, p remains constant along the ray path. However, if lateral velocity gradients or dipping layers are present, then p will change along the ray path.

In a model in which velocity increases with depth, the *travel time curve*, a plot of the first arrival time versus distance, will look like Figure 3.4. Note that p varies along the travel time curve; a different ray is responsible for the “arrival” at each distance X . At any point along a ray, the slowness vector \mathbf{s} can be resolved

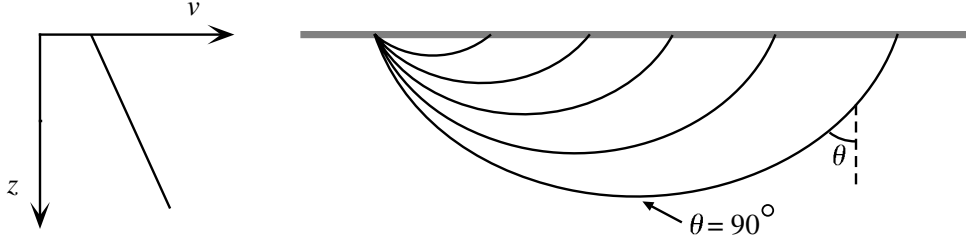


Figure 3.3: Ray paths for a model with a continuous velocity increase with depth will curve back toward the surface. The ray turning point is defined as the lowermost point on the ray path, where the ray direction is horizontal and the incidence angle is 90° .

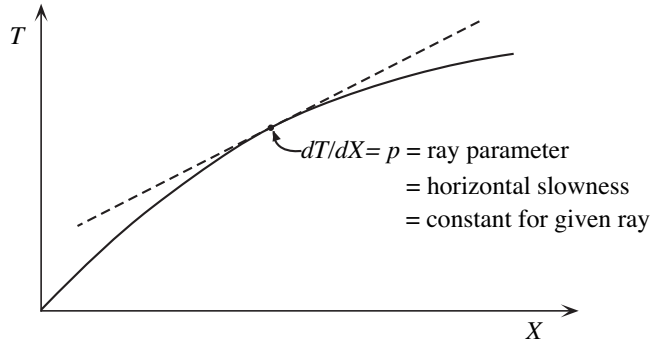


Figure 3.4: A travel time curve for a model with a continuous velocity increase with depth. Each point on the curve results from a different ray path; the slope of the travel time curve, dT/dX , gives the ray parameter for the ray.

into its horizontal and vertical components. The length of \mathbf{s} is given by u , the local slowness. The horizontal component, s_x , of the slowness is the ray parameter p . In an analogous way, we may define the vertical slowness η by

$$\eta = u \cos \theta = (u^2 - p^2)^{1/2}. \quad (3.7)$$

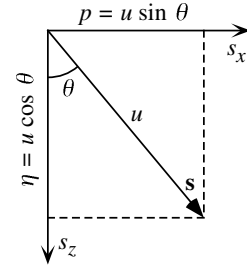
At the turning point, $p = u$ and $\eta = 0$.

We can use these relationships to derive integral expressions to compute travel time and distance along a particular ray². For a surface-to-surface ray path, the total distance $X(p)$ is given by

$$X(p) = 2p \int_0^{z_p} \frac{dz}{(u^2(z) - p^2)^{1/2}}. \quad (3.8)$$

where s_p is the turning point depth. The total surface-to-surface travel time is

$$T(p) = 2 \int_0^{z_p} \frac{u^2(z)}{(u^2(z) - p^2)^{1/2}} dz. \quad (3.9)$$



²See section 4.2 of ITS for details

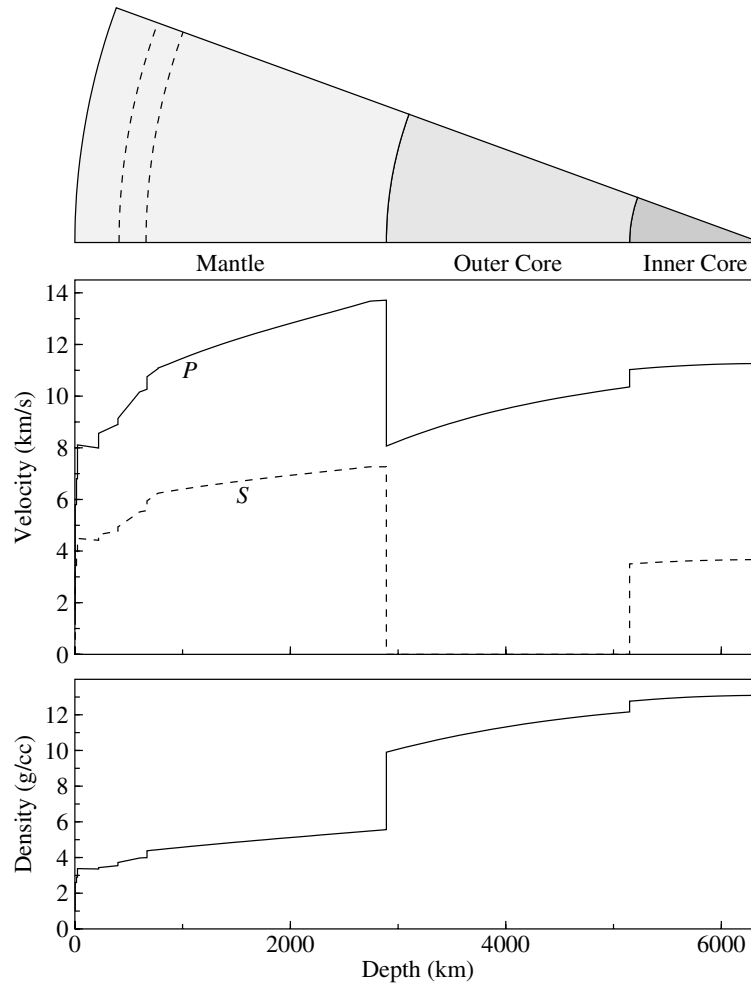


Figure 3.5: Earth's P velocity, S velocity, and density as a function of depth. Values are plotted from the Preliminary Reference Earth Model (PREM) of Dziewonski and Anderson (1981); except for some differences in the upper mantle, all modern Earth models are close to these values. PREM is listed as a table in Appendix 1.

These equations are suitable for a model in which $u(z)$ is a continuous function of depth. The travel times of seismic arrivals can thus be used to determine Earth's average velocity versus depth structure, and this was largely accomplished over fifty years ago. The crust varies from about 6 km in thickness under the oceans to 30–50 km beneath continents. The deep interior is divided into three main layers: the mantle, the outer core, and the inner core (Fig. 3.5). The mantle is the solid rocky outer shell that makes up 84% of our planet's volume and 68% of the mass. It is characterized by a fairly rapid velocity increase in the upper mantle between about 300 and 700 km depth, a region termed the *transition zone*, where several

mineralogical phase changes are believed to occur (including those at the 410- and 660-km seismic discontinuities, shown as the dashed arcs in Fig. 1.1). Between about 700 km to near the core–mantle–boundary (CMB), velocities increase fairly gradually with depth; this increase is in general agreement with that expected from the changes in pressure and temperature on rocks of uniform composition and crystal structure.

3.3 Ray Nomenclature

The different layers in the Earth (e.g., crust, mantle, outer core, and inner core), combined with the two different body wave types (P , S), result in a large number of possible ray geometries, termed *seismic phases*. The following naming scheme has achieved general acceptance in seismology:

3.3.1 Crustal phases

Earth’s crust is typically about 6 km thick under the oceans and 30 to 50 km thick beneath the continents. Seismic velocities increase sharply at the Moho discontinuity between the crust and upper mantle. A P -wave turning within the crust is called Pg , whereas a ray turning in or reflecting off the Moho is called PmP (Fig. 3.6). The m in PmP denotes a reflection off the Moho and presumes that the Moho is a first-order discontinuity. However, the Moho might also be simply a strong velocity gradient, which causes a triplication that mimics the more simple case of a reflection. Finally, Pn is a ray traveling in the uppermost mantle below the Moho. The *crossover point* is where the first arrivals change abruptly from Pg to Pn . The crossover point is a strong function of crustal thickness and occurs at about $X = 30$ km for oceanic

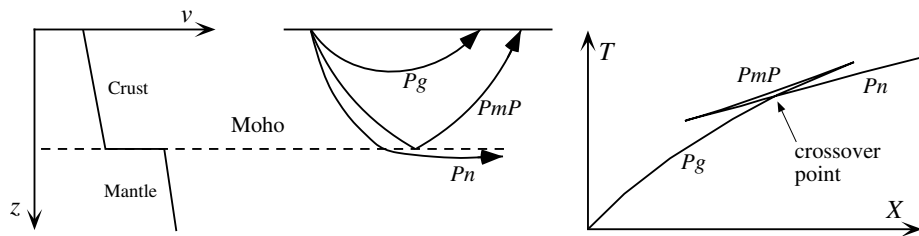


Figure 3.6: Ray geometries and names for crustal P phases. The sharp velocity increase at the Moho causes a triplication in the travel time curve.

crust and at about $X = 150$ km for continental crust. There are, of course, similar names for the S -wave phases (SmS , Sn , etc.) and converted phases such as SmP .

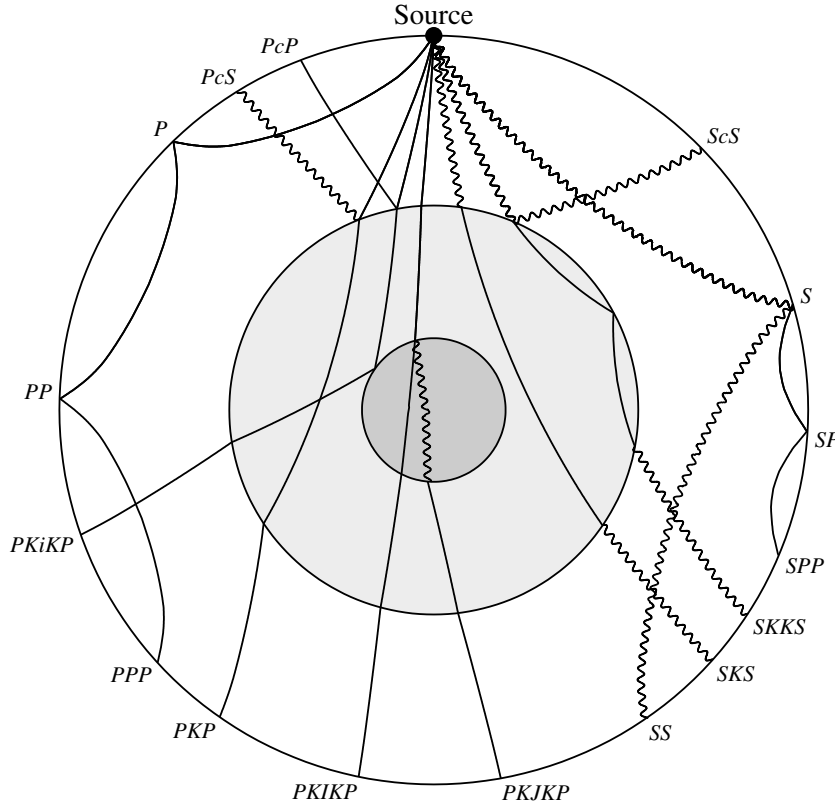


Figure 3.7: Global seismic ray paths and phase names, computed for the PREM velocity model. P -waves are shown as solid lines, S -waves as wiggly lines. The different shades indicate the inner core, the outer core, and the mantle.

3.3.2 Whole Earth phases

Here the main layers are the mantle, the fluid outer core, and the solid inner core.

P - and S -wave legs in the mantle and core are labeled as follows:

P – P -wave in the mantle

K – P -wave in the outer core

I – P -wave in the inner core

S – S -wave in the mantle

J – S -wave in the inner core

c – reflection off the core-mantle boundary (CMB)

i – reflection off the inner core boundary (ICB)

For P - and S -waves in the whole earth, the above abbreviations apply and stand for successive segments of the ray path from source to receiver. Some examples of these ray paths and their names are shown in Figure 3.7. Notice that surface multiple phases are denoted by PP , PPP , SS , SP , and so on. For deep focus earthquakes, the upgoing branch in surface reflections is denoted by a lowercase p or s ; this defines pP , sS , sP , etc. (see Fig. 3.8). These are termed *depth phases*, and the time separation between a direct arrival and a depth phase is one of the best ways to constrain the depth of distant earthquakes. P -to- S conversions can also occur at the CMB; this provides for phases such as PcS and SKS . Ray paths for the core phase PKP are complicated by the Earth's spherical geometry, leading to several triplications in the travel time curve for this phase. Often the inner-core P phase $PKIKP$ is labeled as the df branch of PKP . Because of the sharp drop in P velocity at the CMB, PKP does not turn in the outer third of the outer core. However, S -to- P converted phases, such as SKS and $SKKS$, can be used to sample this region.

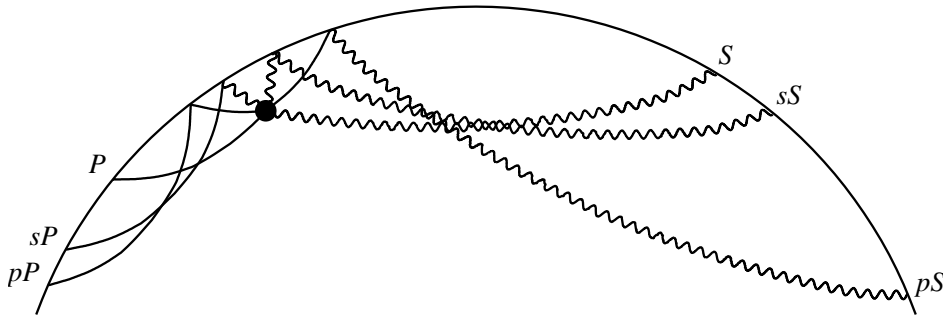


Figure 3.8: Deep earthquakes generate surface-reflected arrivals, termed depth phases, with the upgoing leg from the source labeled with a lower-case p or s . Ray paths plotted here are for an earthquake at 650 km depth, using the PREM velocity model.

3.4 Ray theory and triplications in 1-D Earth models

To first order, the Earth is spherically symmetric, as can be seen in a global stack of long-period seismograms (Fig. 1.3). A variety of seismic body-wave phases result from the P and S wave types and reflections and phase conversions within the Earth. If 3-D heterogeneity were very large, then these phases would not appear so sharp

in a simple stack that combines all source-receiver paths at the same distance.

In the case of spherically symmetric models in which velocity varies only as a function of radius (1-D Earth models), the ray parameter or horizontal slowness p is used to define the ray and can be expressed as:

$$p = u(z) \sin \theta = \frac{dT}{dX} = u_{\text{tp}} = \text{constant for given ray}, \quad (3.10)$$

where $u = 1/v$ is the slowness, z is depth, θ is the ray incidence angle (from vertical), T is the travel time, X is the horizontal range, and u_{tp} is the slowness at the ray turning point.

Generally in the Earth, $X(p)$ will increase as p decreases; that is, as the takeoff angle decreases, the range increases, as shown in Figure 3.9. In this case the derivative dX/dp is negative. When $dX/dp < 0$, we say that this *branch* of the travel time curve is *prograde*. Occasionally, because of a rapid velocity transition in the Earth, $dX/dp > 0$, and the rays turn back on themselves (Fig. 3.10). When $dX/dp > 0$ the travel time curve is termed *retrograde*. The transition from prograde to retrograde and back to prograde generates a *triplication* in the travel time curve.

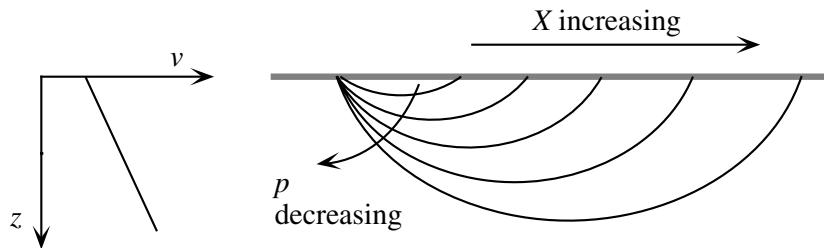


Figure 3.9: A gentle velocity increase with depth causes rays to travel further when they leave the source at steeper angles.

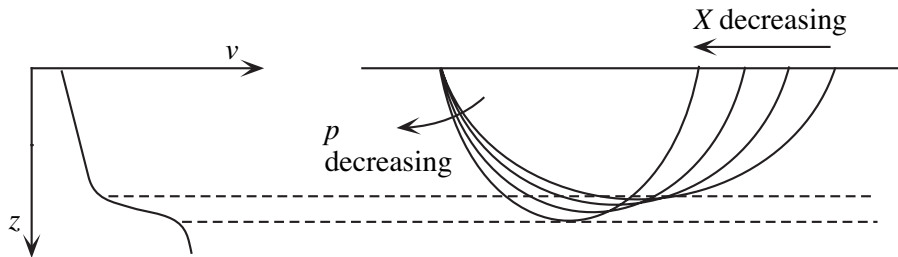


Figure 3.10: A step velocity increase with depth causes steeper rays to fold back on themselves toward the source.

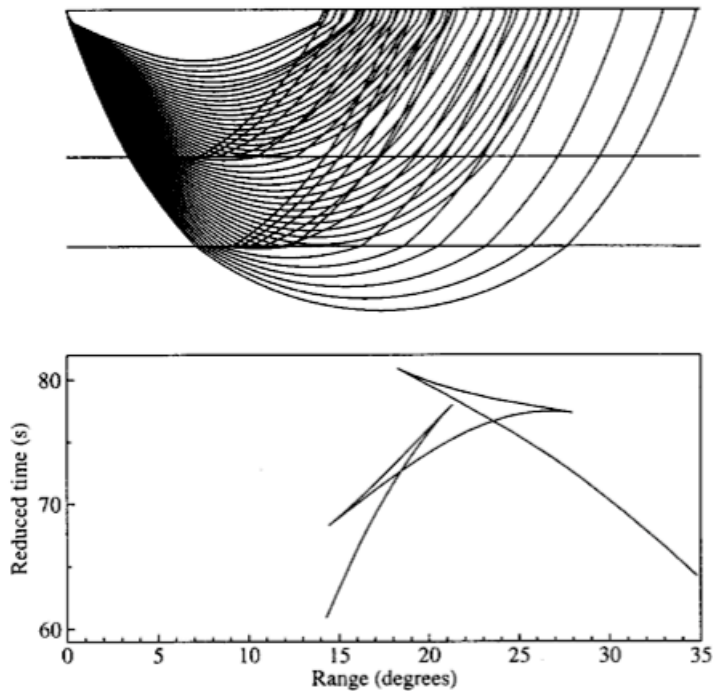


Figure 3.11: The seismic velocity increases near 410 and 660 km depth create a double triplication in the P -wave travel time curve near 20° epicentral distance, as predicted by the IASP91 velocity model (Kennet, 1991). A reduction velocity of 10 km/s is used for the lower plot. From Shearer (2000).

Triplications are very diagnostic of the presence of a steep velocity increase or discontinuity. The 410- and 660-km discontinuities cause a double triplication near 20 degrees (Fig. 3.11 and 3.12), which can be seen in both P waves and S waves. This is how these discontinuities were first discovered in the 1960s. Older studies of the triplications analyzed the timing (and sometimes the slopes, if array data were available) of the different branches of the travel-time curves. However, because the first arriving waves do not directly sample the discontinuities, and the onset times of secondary arrivals are difficult to pick accurately, these data are best examined using synthetic seismogram modeling. The goal is to find a velocity-depth profile that predicts theoretical seismograms that match the observed waveforms. This inversion procedure is difficult to automate, and most results have been obtained using trial-and-error forward modeling approaches.

An advantage of this type of modeling is that it often provides a complete velocity

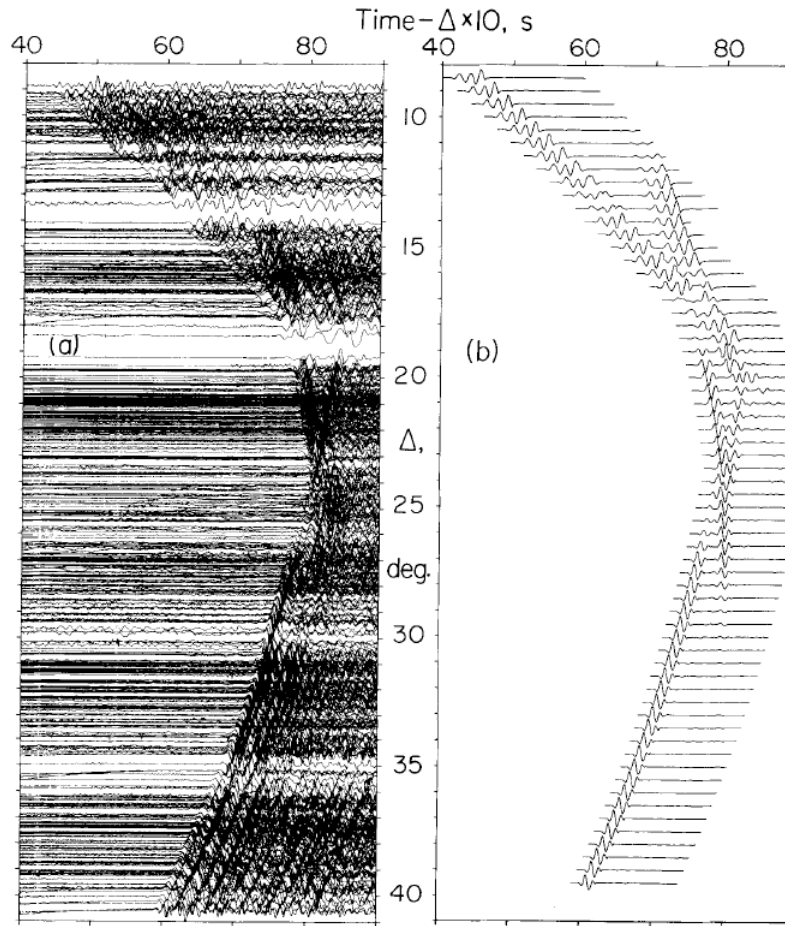


Figure 3.12: Record section of P waves from Mexican earthquakes recorded by southern California seismic stations (left) compared to synthetic seismograms. From Walck (1984).

versus depth function extending from the surface through the transition zone. Thus, in principle, some of the tradeoffs between shallow velocity structure and discontinuity depth that complicate analysis of reflected and converted phases (see below) are removed. However, significant ambiguities remain. It is difficult to derive quantitative error bounds on discontinuity depths and amplitudes from forward modeling results. Tradeoffs are likely between the discontinuity properties and velocities immediately above and below the discontinuities—regions that are not sampled with first-arrival data. The derived models tend to be the simplest models that are found to be consistent with the observations. In most cases, the 410 and 660 discontinuities are first-order velocity jumps, separated by a linear velocity gradient. However,

velocity increases spread out over 10 to 20 km depth intervals would produce nearly identical waveforms (except in the special case of pre-critical reflections), and subtle differences in the velocity gradients near the discontinuities could be missed. The data are only weakly sensitive to density; thus density, if included in a model, is typically derived using a velocity versus density scaling relationship.

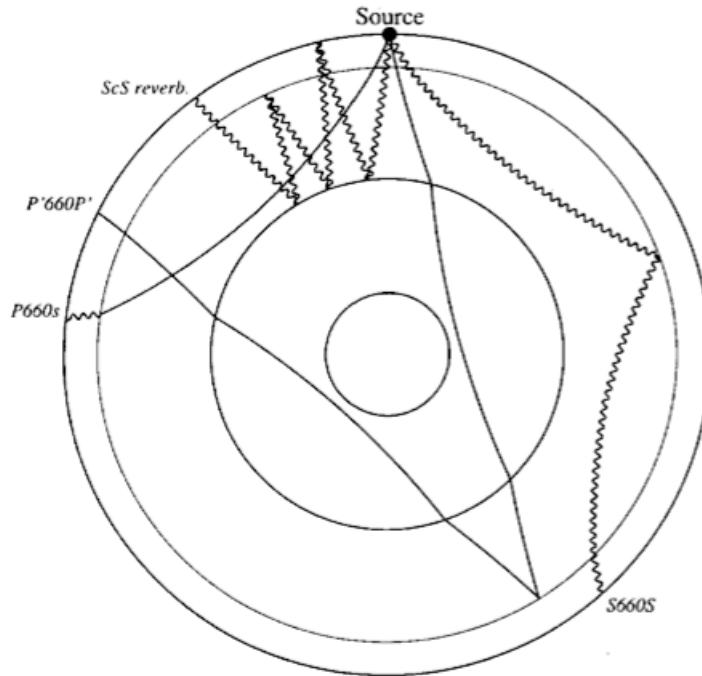


Figure 3.13: Example ray paths for discontinuity phases resulting from reflections or phase conversions at the 660-km discontinuity. P waves are shown as smooth lines, S waves as wiggly lines. The ScS reverberations include a large number of top- and bottom-side reflections, only a single example of which is plotted. From Shearer (2000).

3.5 Discontinuity phases

An alternative approach to investigating upper mantle discontinuity depths involves the study of minor seismic phases that result from reflections and phase conversions at the interfaces. These can take the form of P or S topside and bottomside reflections, or P -to- S and S -to- P converted phases. The ray geometry for many of these phases is shown in Figure 3.13. Typically these phases are too weak to ob-

serve clearly on individual seismograms, but stacking techniques (the averaging of results from many records) can be used to enhance their visibility. Analysis and interpretation of these data have many similarities to techniques used in reflection seismology.

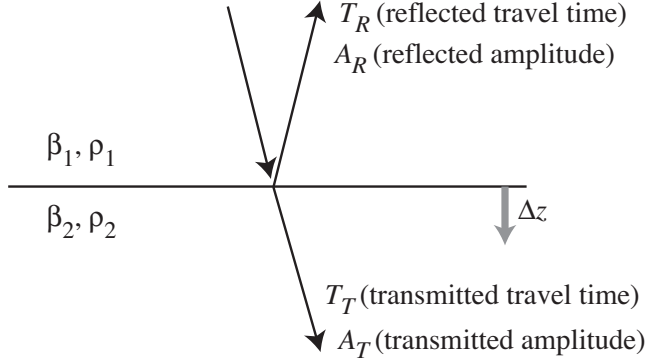


Figure 3.14: Ray geometry for near-vertical S -wave reflection and transmission.

Note that these reflected and converted waves are much more sensitive to discontinuity properties than directly transmitted waves. For example, consider the reflected and transmitted waves for an S -wave incident on a discontinuity (Fig. 3.14). For near-vertical incidence, the travel time perturbation for the reflected phase is approximately

$$\Delta T_R = \frac{2\Delta z}{\beta_1} \quad (3.11)$$

where Δz is the change in the layer depth and β_1 is the velocity of the top layer. The travel time perturbation for the transmitted wave is

$$\begin{aligned} \Delta T_T &= \frac{\Delta z}{\beta_1} - \frac{\Delta z}{\beta_2} = \Delta z \left(\frac{1}{\beta_1} - \frac{1}{\beta_2} \right) = \Delta z \left(\frac{\beta_2 - \beta_1}{\beta_1 \beta_2} \right) = \frac{\Delta z}{\beta_1} \frac{\beta_2 - \beta_1}{\beta_2} \\ &= \frac{1}{2} \frac{\beta_2 - \beta_1}{\beta_2} \Delta T_R \end{aligned} \quad (3.12)$$

where β_2 is the velocity in the bottom layer. Note that for a 10% velocity jump, $(\beta_2 - \beta_1)/\beta_2 \approx 0.1$, and the reflected travel time T_R is 20 times more sensitive to discontinuity depth changes than the transmitted travel time T_T .

Now consider the amplitudes of the phases. At vertical incidence, assuming an incident amplitude of one, the reflected and transmitted amplitudes are given by

the S -wave reflection and transmission coefficients are

$$A_R = \frac{\dot{S}\dot{S}_{\text{vert}}}{\dot{S}\dot{S}_{\text{vert}}} = \frac{\rho_1\beta_1 - \rho_2\beta_2}{\rho_1\beta_1 + \rho_2\beta_2}, \quad (3.13)$$

$$A_T = \frac{\dot{S}\dot{S}_{\text{vert}}}{\dot{S}\dot{S}_{\text{vert}}} = \frac{2\rho_1\beta_1}{\rho_1\beta_1 + \rho_2\beta_2}. \quad (3.14)$$

where ρ_1 and ρ_2 are the densities of the top and bottom layers, respectively. The product $\beta\rho$ is termed the shear impedance of the rock. A typical upper-mantle discontinuity might have a 10% impedance contrast, i.e., $\Delta\rho\beta/\overline{\rho\beta} = 0.1$. In this case, $\dot{S}\dot{S} = -0.05$ (assuming $\beta_1\rho_1 < \beta_2\rho_2$) and $\dot{S}\dot{S} = 0.95$. The transmitted wave is much higher amplitude and will likely be easier to observe. But the reflected wave, if it can be observed, is much more sensitive to changes in the discontinuity impedance contrast. If the impedance contrast doubles to 20%, then the reflected amplitude also doubles from 0.05 to 0.1. But the transmitted amplitude is reduced only from 0.95 to 0.9, a 10% change in amplitude that will be much harder to measure. Because the reflected wave amplitude is directly proportional to the impedance change across the discontinuity, I will sometimes refer to the impedance jump as the “brightness” of the reflector.

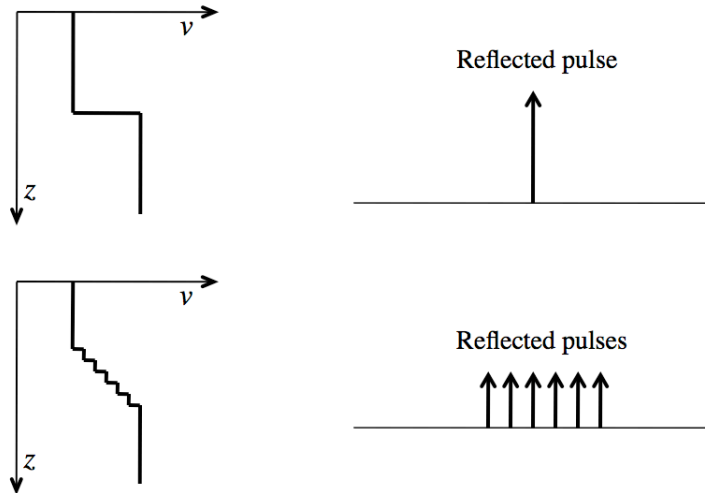


Figure 3.15: A step velocity discontinuity produces a delta-function reflected pulse. A series of velocity jumps produces a series of delta-function reflections.

Another important discontinuity property is the sharpness of the discontinuity, that is over how narrow a depth interval the rapid velocity increase occurs. This

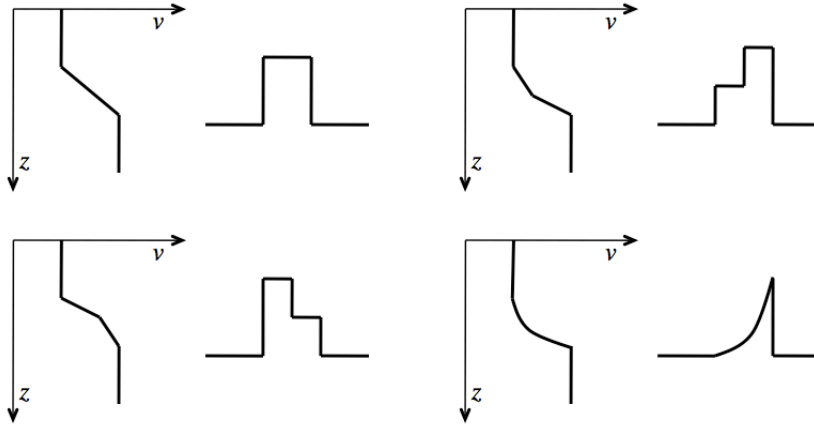


Figure 3.16: Different velocity-depth profiles and their top-side reflected pulses.

property can be detected in the possible frequency dependence of the reflected phase. A step discontinuity reflects all frequencies equally and produces a delta-function reflection for a delta-function input (Fig. 3.15, top). In contrast, a velocity gradient will produce a box car reflection. To see this, first consider a staircase velocity depth function (Fig. 3.15, bottom). Each small velocity jump will produce a delta function reflection.

In the limit of small step size, the staircase model becomes a continuous velocity gradient, and the series of delta functions become a boxcar function (top left of Fig. 3.16). This acts as a low pass filter that removes high-frequency energy. Thus, the sharpness of a discontinuity can best be constrained by the highest frequencies that are observed to reflect off it. The most important evidence for the sharpness of the upper-mantle discontinuities is provided by observations of short-period precursors to $P'P'$. Underside reflections from both the 410 and 660 discontinuities are visible to maximum frequencies, f_{max} , of ~ 1 Hz (sometimes slightly higher). The 520 -km discontinuity is not seen in these data, even in data stacks with excellent signal-to-noise (Benz and Vidale, 1993), indicating that it is not as sharp as the other reflectors.

$P'P'$ precursor amplitudes are sensitive to the P impedance contrast across the discontinuities. Relatively sharp impedance increases are required to reflect high-frequency seismic waves. This can be quantified by computing the reflection coefficients as a function of frequency for specific models. If simple linear impedance

gradients are assumed, these results suggest that discontinuity thicknesses of less than about 5 km are required to reflect observable P waves at 1 Hz (e.g., Richards, 1972; Lees et al., 1983), a constraint confirmed using synthetic seismogram modeling (Benz and Vidale, 1993). A linear impedance gradient of thickness h will act as a low pass filter to reflected waves. At vertical incidence this filter is closely approximated by convolution with a boxcar function of width $t_w = 2h/v$, where t_w is the two-way travel time through the discontinuity and v is the wave velocity. The frequency response is given by a sinc function, the first zero of which occurs at $f_0 = 1/t_w$. We then have $h = v/2f_0 = \lambda/2$, where λ is the wavelength; the reflection coefficient becomes very small as the discontinuity thickness approaches half the wavelength.

Interpretation of $P'P'$ precursor results is further complicated by the likely presence of non-linear velocity increases, as predicted by models of mineral phase changes (e.g., Stixrude, 1997). The reflected pulse shape (assuming a delta-function input) will mimic the shape of the impedance profile (Fig. 3.16). In the frequency domain, the highest frequency reflections are determined more by the sharpness of the steepest part of the profile than by the total layer thickness. In principle, resolving the exact shape of the impedance profile is possible, given broadband data of sufficient quality. However, the effects of noise, attenuation and band-limited signals make this a challenging task. Recently, Xu et al. (2003) analyzed $P'P'$ observations at several short-period arrays and found that the 410 reflection could be best modeled as a 7-km-thick gradient region immediately above a sharp discontinuity. Figure 3.17 shows some of their results, which indicate that the 660 is sharper (less than 2 km thick transition) than the 410 because it can be observed to higher frequency. The 520-km discontinuity is not seen in their results at all, indicating that any P impedance jump must occur over 20 km or more.

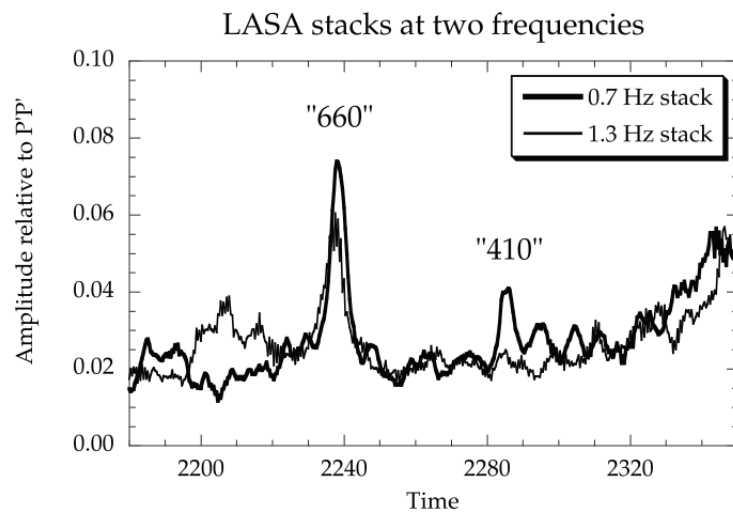


Figure 3.17: LASA envelope stacks of nine events at two different frequencies.

Chapter 4

Tutorial: Modeling SS precursors

The upper-mantle discontinuities provide important constraints on models of mantle composition and dynamics. The most established mantle seismic discontinuities occur at mean depths near 410, 520, and 660 km and will be a focus of this exercise. For want of better names, they are identified by these depths, which are subject to some uncertainty (the older literature sometimes will refer to the 400, 420, 650, 670, etc.). Furthermore it is now known that these features are not of constant depth, but have topography of tens of kilometers. The term “discontinuity” has traditionally been applied to these features, although they may involve steep velocity gradients rather than first-order discontinuities in seismic velocity. The velocity and density jumps at these depths result primarily from phase changes in olivine and other minerals, although some geophysicists, for geochemical and various other reasons, argue for small compositional changes near 660 km.

The mantle is mainly composed of olivine (Mg_2SiO_4), which undergoes phase changes near 410, 520 and 660 km (see Fig. 4.1). The sharpness of the seismic discontinuities is related to how rapidly the phase changes occur with depth. Generally the *660* is thought to be sharper than the *410*. The *520* is likely even more gradual, so much that it does not yet appear in most standard 1-D Earth models.

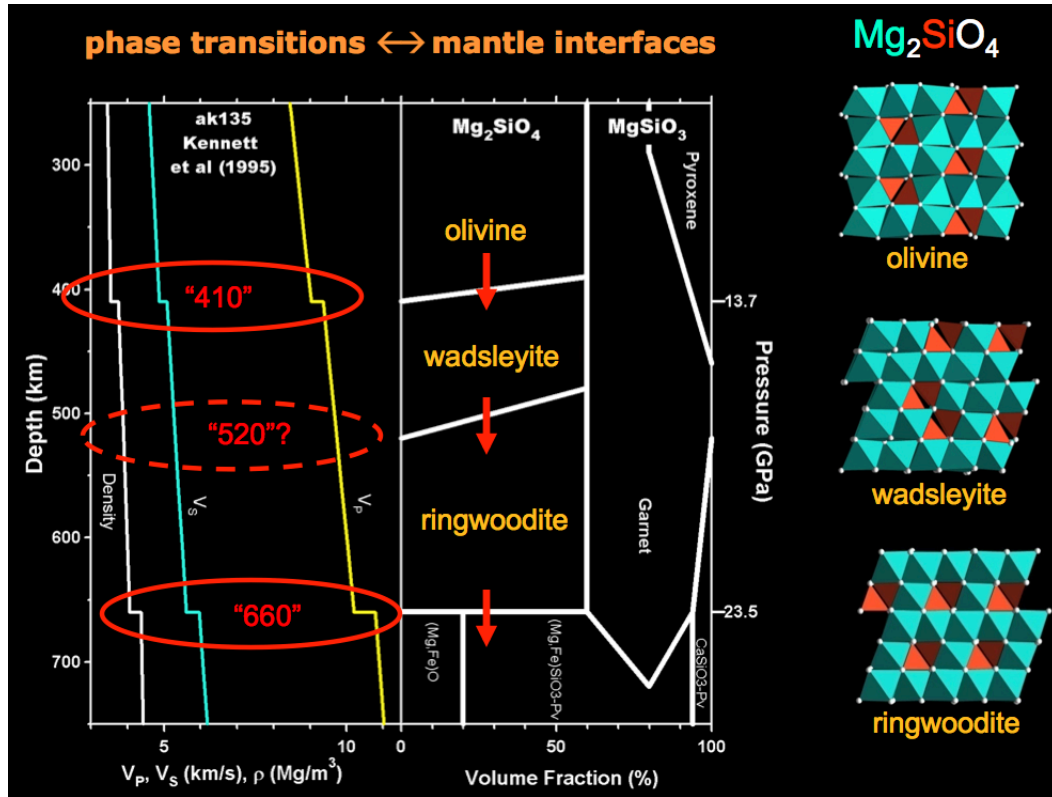


Figure 4.1: Seismic velocity and density (left) compared to mantle composition (right). Figure courtesy of Rob van der Hilst.

4.1 SS precursors

A useful dataset for global analysis of upper-mantle discontinuity properties is provided by *SS* precursors. These are most clearly seen in global images when *SS* is used as a reference phase (see Fig. 4.2).

SS precursors are especially valuable for global mapping because of their widely distributed bouncepoints, which lie nearly halfway between the sources and receivers (see Fig. 4.3). The timing of these phases is sensitive to the discontinuity depths below the *SS* surface bouncepoints. *SS* precursors cannot be reliably identified on individual seismograms, but the data can be grouped by bouncepoint to perform stacks that can identify regional variations in discontinuity tomography. The measured arrival times of the 410- and 660-km phases (termed *S410S* and *S660S*, respectively) can then be converted to depth by assuming a velocity model. The topography of the 660-km discontinuity measured in this way is shown in Figure 4.4.

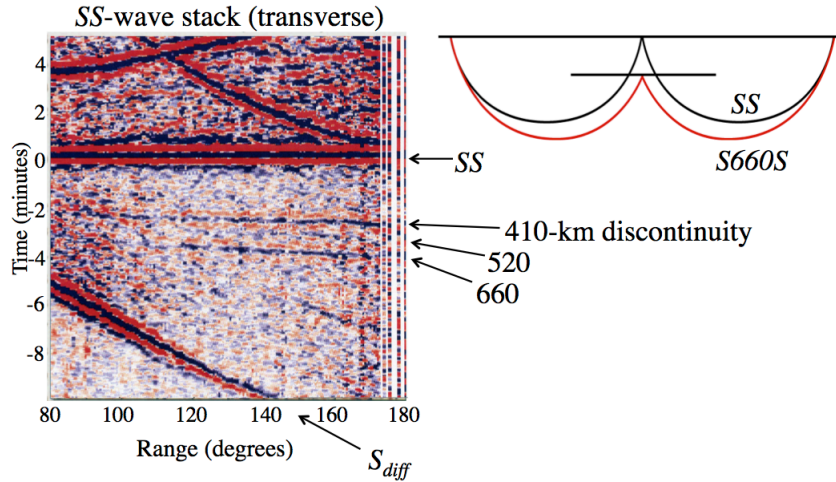


Figure 4.2: Stacked images of long-period GSN data from shallow sources (< 50 km) obtained using SS as a reference. From Shearer (1991).

Only long horizontal wavelengths can be resolved because of the broad sensitivity of the long-period SS waves to structure near the bouncepoint. The most prominent features in this map are the troughs in the 660 that appear to be associated with subduction zones.

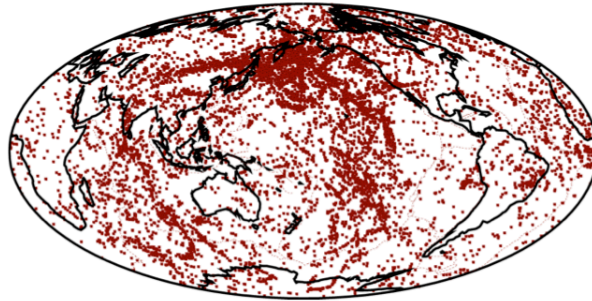


Figure 4.3: The global distribution of SS bouncepoints. From Flanagan and Shearer (1998).

High-pressure mineral physics experiments have shown that the olivine phase change near 660 km has what is termed a negative *Clapeyron slope*, which defines the expected change in pressure with respect to temperature. A negative slope means that an increase in depth (pressure) should occur if there is a decrease in temperature. Thus these results are consistent with the expected colder temperatures in subduction zones. It appears that in many cases slabs are deflected horizontally

by the 660-km phase boundary (students should think about why the *660* tends to resist vertical flow) and pool into the transition zone. Tomography results show this for many of the subduction zones in the northwest Pacific (see Fig. 4.5). However, in other cases tomography results show that the slabs penetrate through the *660*. This would cause a narrow trough in the *660* that would be difficult to resolve with the *SS* precursors.

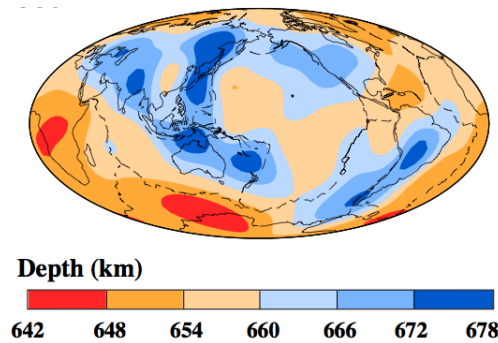


Figure 4.4: Long wavelength topography on the 660-km discontinuity as measured using *SS* precursors. From Flanagan and Shearer (1998).

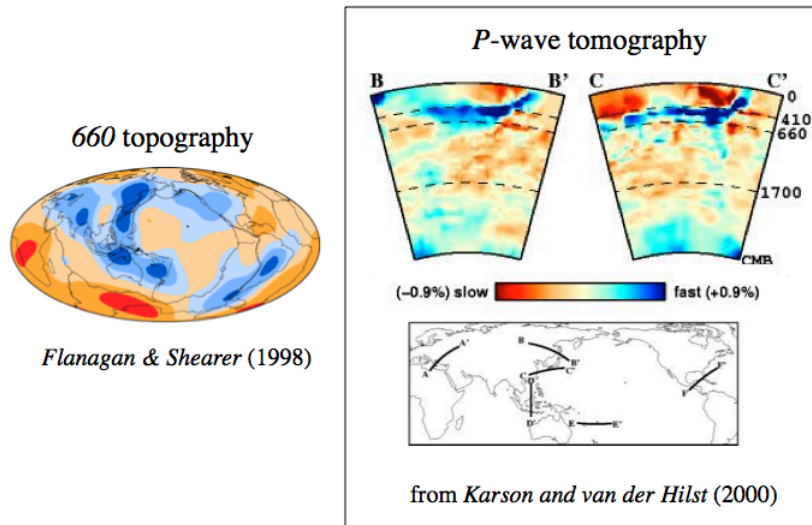


Figure 4.5: A comparison between long wavelength topography on the 660-km discontinuity as measured using *SS* precursors and transition zone velocity structure from seismic tomography.

4.2 Oceanic stack example

One purpose of this exercise will be to reproduce some of the results of Shearer (1996), who modeled *SS* precursor results to confirm the existence of the 520-km discontinuity and to model its properties. Because Moho reflections can distort the shape of the *SS* pulse, only oceanic bouncepoints were used, where the shallow crustal thickness has minimal effect on the waveforms. Figure 4.6 shows the resulting waveform stack, which has clear peaks from the 410- and 660-km discontinuities.

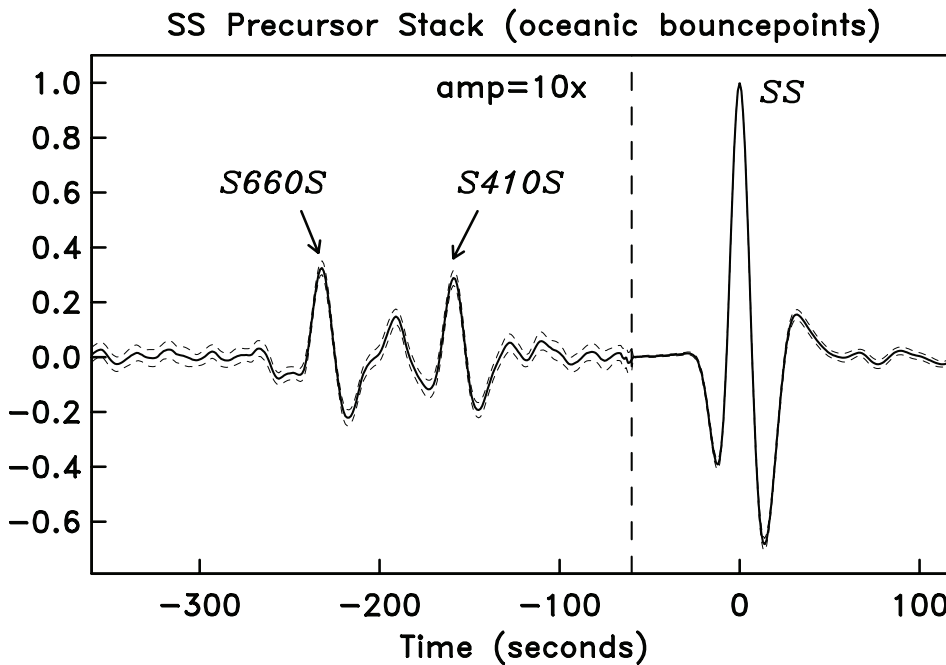


Figure 4.6: A stack of *SS* precursors in 1142 transverse-component seismograms between 120° and 160° range, showing peaks from the underside reflected phases *S660S* and *S410S*. The precursors are stacked along the predicted travel time curve for a reflector at 550 km and adjusted to a reference range of 138° . *SS* is stacked separately and scaled to unit amplitude; the precursor amplitudes are exaggerated by a factor of 10 for plotting purposes. The 95% confidence limits, shown as dashed lines, are calculated using a bootstrap resampling technique. Note the peak between the 410- and 660-km peaks, suggesting an additional reflector at 520 km depth.

The computer program PLAYMOD is designed to compute synthetic reflection pulses to model this waveform stack using a graphical user interface (GUI) so that the user can interactively explore different *S*-wave velocity models (see appendix for details of how to get the software to work). The synthetics involve the following

steps:

1. Ray trace through the velocity model for a range of values of the ray parameter p and for a range of hypothetical reflectors in the upper mantle. This provides travel time and geometrical spreading amplitude information for the reference *SS* phase and any underside reflections.
2. Compute underside reflection coefficients for the velocity changes with depth in the model, assuming a constant velocity versus density scaling relationship. Combine with the geometrical spreading information to produce ray theoretical amplitudes for the precursors relative to the reference *SS* phase.
3. Convolve the synthetic time series with a reference wavelet, defined by the main *SS* pulse.
4. Convolve the synthetics with a Gaussian function to account for the travel-time perturbations induced by upper-mantle velocity heterogeneity and discontinuity topography. A standard deviation of 2.5 s was assumed in Shearer (1996).

Note that for simplicity no corrections are applied for attenuation or for the predicted effect of the oceanic crust on the *SS* waveform. These corrections were included in Shearer (1996) but have a relatively minor effects.

PLAYMOD will display a plot of the velocity-depth function on the left side of the screen, the predicted surface-to-surface travel time residuals relative to the ak135 model, and the fit of the synthetic *SS* precursor waveforms. The residuals are included to show how sensitive the model is to small changes. Globally averaged travel time observations show variations of less than 1 to 2 seconds. Thus models can be excluded that produce travel time residuals that exceed these limits.

Within PLAYMOD, the user inputs changes using a three-button mouse. The mouse input numbering scheme is as follows: (1) left click, (2) middle click, (3) right click, (4) shift-left click, (5) shift-middle click, (6) shift-right click. The user can change the model by left clicking on one of the $V(Z)$ points. A middle click will delete one of the points. A right click will add another point. To zoom in or

out on the $V(Z)$ plot, shift-left click, To output the model to a file (out.vzmod), shift-middle click. To quit the program, shift-right click.

For the tutorial, your tasks are as follows:

1. Find a model that fits the oceanic SS precursor stack without violating the ak135 travel time constraint. Does this model have a 520-km discontinuity? What happens if you change the velocity gradient immediately below the 660-km discontinuity?
2. Revenaugh and Sipkin (1994) found seismic evidence for low S -wave velocities immediately above the 410-km discontinuity from ScS reverberations along corridors within the western Pacific subduction zones. They modeled their results with a 6% impedance decrease at 330 km depth, suggesting that this was a region of silicate partial melt. Explore the implications of their model on the SS precursor waveforms¹. Could such an anomaly be detected using a more focused SS waveform stack for these subduction zones?
3. Tackley (2002) showed that any compositional discontinuity in the deep mantle would create a boundary layer in the convection flow with strong volumetric heterogeneity that should be seismically detectable. Explore the effect of a small (1%) discontinuity in seismic velocity in the lower mantle on seismic travel times.

4.3 Appendix

The folder/directory ALL_PLAYMOD contains all the required programs. You will need compatible C and F90 compilers. Here are the steps to compile everything.

1. Compile the leolib screen plotting routines by entering 'makeleo' in XPLOT/LEOLIB. You may need to replace gcc and gfortran with your own compilers. However, note that the C and Fortran compilers must be compatible and you must use a F90 compiler (because playmod is written in F90). You will likely get lots of

¹A complication is that the constant velocity versus density scaling assumed in PLAYMOD cannot be true for a low velocity zone (since density never decreases substantially with depth). As a kludge, assume a 3% S-velocity drop with depth.

warnings about improper use of 'malloc' and other built-in functions. Ignore these!

2. Compile the ezxplot screen plotting Fortran routines by entering 'ezxplot.bld' in XPLOT. You may need to replace gfortran with your own Fortran90 compiler. You may get lots of warnings about the improper use of real numbers in do loops. If you are interested, documentation for ezxplot is in ezxplot.man. It's a good idea at this point to also compile and run the test program teste-zxplot.f to see if the screen plotting works. There is a Makefile to do this. Note that you MUST be running X11 on the Macs.
3. Compile playmod by entering playmod.bld in ALL_PLAYMOD.
4. Run playmod by entering do.playmod in ALL_PLAYMOD.

4.4 References

Revenaugh, J., and S. A. Sipkin, Seismic evidence for silicate melt atop the 410-km mantle discontinuity, *Nature*, **369**, 474–476, 1994.

Shearer, P. M., Transition zone velocity gradients and the 520-km discontinuity, *J. Geophys. Res.*, **101**, 3053–3066, 1996.

Tackley, P. J., Strong heterogeneity caused by deep mantle layering, *Geochem. Geophys. Geosys.*, **3**, doi 10.1029/2001GC000167.